

Ultra-broadband Mid to Long-wave Infrared Spintronic Poisson Bolometer

Mohamed A. Mousa,^{†,‡} Leif Bauer,^{†,‡} Daien He,^{†,‡} Sakshi Gupta,^{‡,¶} Shubhankar Jape,^{†,‡} Utkarsh Singh,^{†,‡} Bhagwati Prasad,[§] Partha P. Mukherjee,^{||} Angshuman Deka,[‡] and Zubin Jacob^{*,†,‡}

[†]*Elmore Family School of Electrical and Computer Engineering, Purdue University, West Lafayette, IN 47907, USA*

[‡]*Birck Nanotechnology Center, Purdue University, West Lafayette, IN 47907, USA*

[¶]*Department of Physics and Astronomy, Purdue University, West Lafayette, IN 47907, USA*

[§]*Department of Materials Engineering, Indian Institute of Science, Bangalore, KA, 560012, India*

^{||}*School of Mechanical Engineering, Purdue University, West Lafayette, IN 47907, USA*

E-mail: zjacob@purdue.edu

Abstract

Infrared detectors have traditionally been divided into two fundamental classes, mid-wave (MWIR, 3-5 μm) and long-wave (LWIR, 8-14 μm). Integrating MWIR and LWIR within a single device is challenging due to distinct materials, cooling needs, and detection mechanisms, while such integration is critical for improved object recognition, temperature estimation, and environmental sensing. In this work, we demonstrate a Spintronic Poisson (SP) bolometer enabling room-temperature ultra-broadband sensing across 3-14 μm . Unlike conventional bolometers that rely on continuous analog sig-

nals, the SP bolometer implements a Poisson-counting detection paradigm, encoding temperature in discrete stochastic events, which turns thermal noise from a limitation into the basis of the estimator itself. We fabricate the SP bolometer using a spintronic transduction layer integrated with a plasmonic nanoantenna array to enhance broadband infrared absorption. Using spintronic transduction, the device achieves the noise-equivalent temperature difference (NETD, thermal sensitivity metric) of $\approx 80\text{--}100$ mK at 300 K, surpassing uncooled detectors and approaching cooled technologies. This work establishes a statistical detection paradigm for room-temperature infrared sensing with broad application potential.

Introduction

Thermal infrared (IR) detection is limited to two detector classes, mid-wave (MWIR, $3\text{--}5\mu\text{m}$) and long-wave (LWIR, $8\text{--}14\mu\text{m}$). MWIR photodetectors based on HgCdTe or InSb typically require cryogenic cooling to suppress dark current and achieve high sensitivity.^{1\text{--}6} Many LWIR imagers use uncooled microbolometer focal-plane arrays based on vanadium-oxide (VO_x) or amorphous silicon thermistor films.^{7\text{--}10} These two technologies rely on fundamentally different material systems, such as narrow-bandgap semiconductors versus VO_x -based resistive films, and different detection mechanisms. These differences have historically prevented coherent integration of the two approaches within a single device, limiting the development of ultra-broadband infrared sensors necessary for next-generation AI-driven remote sensing¹¹ and environmental monitoring.¹²

This broadband detection enables precise temperature estimation,¹³ reliable material differentiation,^{14,15} and robust target identification in complex environments.^{16,17} Capturing information across multiple bands provides complementary insights. MWIR offers high-contrast thermal imaging, particularly for high-temperature targets,^{18,19} and LWIR excels at resolving fine temperature differences in or near ambient-temperature scenes.²⁰ These combined capabilities are essential for precise thermal object-detection,²¹ neural thermal

imaging,²² predictive diagnostics such as early detection of solid-state battery failures,²³ gas detection,²⁴ and heat-assisted detection and ranging (HADAR).²⁵

Despite significant advances, achieving simultaneous MWIR–LWIR detection within a single compact, high-performance pixel device remains a critical challenge. Conventional dual-band MWIR–LWIR sensors rely on heterogeneous stacks or hybrid optical paths, introducing cross-talk and transmission losses.^{26,27} Lattice and bandgap mismatches between MWIR and LWIR materials hinder monolithic integration and reduce quantum efficiency.³ At the system level, most high-sensitivity MWIR detectors require cryogenic cooling, whereas LWIR detectors operate uncooled, creating noise mismatches and increasing size, weight, and power (SWaP) demands.²⁸ These limitations prevent the realization of ultra-broadband (3–14 μm) systems that combine high thermal sensitivity (< 100mK), high speed (> 50Hz), and room-temperature (300 K) operation on a single chip.

Recent efforts to achieve ultra-broadband infrared detection have explored both mature and emerging material technologies. Conventional detectors based on HgCdTe (MCT)^{39,40} and type-II superlattices⁴¹ offer high performance but are limited by complex fabrication, low yield, high SWaP, and cooling requirements. Strained layer superlattice (SLS) architectures³⁵ have demonstrated dual-band MWIR/LWIR detection with improved uniformity and reduced dark current, however they still require complex epitaxial growth and cooling requirements (120-170K). Stacked colloidal quantum dots (CQDs)³³ achieve tunable SWIR–MWIR dual-band detection through size-controlled PbS and PbSe layers, providing spectral tuning and reduced crosstalk, but remain constrained by fabrication complexity and cryogenic cooling (85K). Carbon nanotube (CNT) films offer broadband absorption from the ultraviolet to the terahertz range,²⁹ but low thermal sensitivity and integration challenges have limited their use in high-resolution imaging.

Beyond material and architectural advances, a fundamental limitation of conventional infrared bolometers lies in the detection mechanism itself. Traditional bolometric sensors infer temperature changes from continuous analog readouts such as resistance, voltage, or

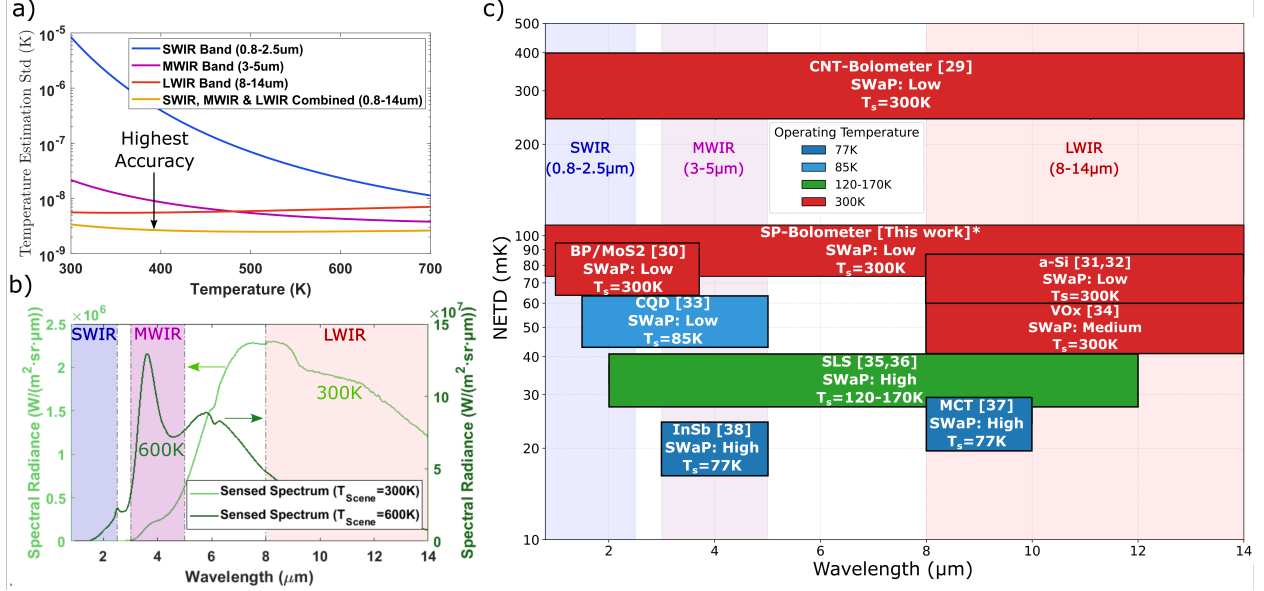


Figure 1: Ultra-broadband SP-bolometer performance and comparison with state-of-the-art infrared detectors. (a) Ultra-broadband sensed spectrum of the SP-bolometer, where light green is at a scene temperature of 300K, and dark green is at a scene temperature of 600K. (b) Temperature estimation standard deviation (square root of Cramer-Rao bound (CRB)) for the SWIR, MWIR, LWIR, and the SWIR-MWIR-LWIR combined cases. Ultra-broadband combined achieves the lowest CRB (i.e., the lowest standard deviation), indicating superior accuracy compared to single-band configurations. (c) Performance comparison of infrared detectors showing noise-equivalent temperature difference (NETD) versus wavelength for different technologies. Lower NETD means higher thermal sensitivity. Colored bars indicate operating temperatures (see legend), with labels showing detector name, SWaP, and Sensor temperature. SWaP: size, weight, and power. The Spintronic Poisson bolometer (SP, this work) achieves room-temperature operation across 0.8-14 μm with 80-100 mK NETD. CNT: Carbon nanotube,²⁹ BP/MoS₂: Black Phosphorus on top of Molybdenum Disulfide,³⁰ a-Si: Amorphous Silicon,^{31,32} CQD: colloidal quantum dots,³³ VOx: Vanadium Oxide,³⁴ SLS: Strained Layer Superlattice,^{35,36} MCT: Mercury Cadmium Telluride,³⁷ InSb: Indium Antimonide.³⁸ *MWIR and LWIR are experimentally characterized in this work, while SWIR performance is estimated.

current, whose estimation accuracy at room temperature is fundamentally constrained by thermal fluctuation noise,⁴² electronic readout noise,⁴³ and low-frequency noise.⁴⁴ Here, we introduce the Poisson bolometer, a distinct regime of bolometric operation in which infrared-induced temperature changes are estimated from variations in the mean rate of discrete output events generated by an intrinsically stochastic physical process.^{45,46} This approach is fundamentally different from photon counting. The detected events do not correspond to individual photons, but arise from thermally driven dynamics whose statistics follow a Poisson distribution.^{47,48}

In this model, the event counts N in a fixed measurement interval follow a Poisson probability mass function,

$$P(N, 0) = \frac{\lambda_0^N e^{-\lambda_0}}{N!}, \quad (1)$$

for baseline conditions (room temperature) with mean event rate λ_0 , N is the number of detected stochastic events, and

$$P(N, I_{\text{BB}}) = \frac{\lambda_{\text{BB}}^N e^{-\lambda_{\text{BB}}}}{N!}, \quad (2)$$

under blackbody illumination of intensity I_{BB} . Here, λ_{BB} is the mean event rate increased by absorbed infrared power, which scales linearly with I_{BB} ,⁴⁹ establishing a statistical framework in which temperature can be estimated directly from the mean count of stochastic events.

By encoding temperature information in discrete event counts rather than continuous signal amplitudes, the Poisson bolometer inherently operates under stochastic fluctuations present at room temperature. These fluctuations increase or decrease depending on how the detected temperature deviates from room temperature. In this regime, thermal noise is not a limitation but forms the basis of the estimator itself.^{46,50} Importantly, this Poisson-counting regime is independent of any specific material system or device architecture and can be realized by a broad class of bolometric structures that support Poisson-distributed event generation.

One realization of the Poisson-bolometer operating regime is achieved using spintronic materials.⁵¹ In this platform, infrared-induced photothermal heating modulates stochastic magnetic switching processes, enabling direct transduction into discrete electrical events with Poisson statistics. Leveraging this operating principle, we implement the Spintronic Poisson (SP) bolometer, which couples spintronic transduction with engineered optical absorption to overcome the bandgap-limited spectral response of conventional infrared detectors. This approach decouples spectral response from material bandgap constraints, enabling continuous MWIR–LWIR sensing within a single nanoscale device without the need for cryogenic cooling and, building on this principle, achieves ultra-broadband sensitivity across 3–14 μm with measured thermal sensitivity of 80–100 mK at room temperature. The core scientific advance lies in coupling Poisson-based spintronic readout with engineered optical absorption, enabling broadband spectral coupling, high-speed operation, and compatibility with chip-scale integration.

Building on this principle, the SP bolometer achieves ultra-broadband sensitivity across 3–14 μm with measured thermal sensitivity of 80–100 mK at room temperature. A nanoplasmonic antenna array positioned above the active region enhances infrared absorption and provides tunable spectral selectivity through controlled geometry and material design. The $300\text{nm} \times 300\text{nm}$ active area enables sub-wavelength pixel footprints ($< 10\mu\text{m}$), which are difficult to achieve in conventional MWIR and LWIR technologies limited by the thermal capacitance of the microbolometer element and its thermal time constant.⁵² Smaller pixels reduce responsivity due to reduced absorber area and limited heat capacity.⁵³ Figure 1a demonstrates through a Cramér–Rao-bound analysis that jointly exploiting SWIR, MWIR, and LWIR measurements substantially improves temperature-estimation accuracy because each spectral band contributes complementary information (see Supplementary Section I), and Figure 1b shows the resulting broadband absorption response under 300 K and 600 K blackbody illumination.

To benchmark the performance of the SP bolometer, we conducted a comprehensive

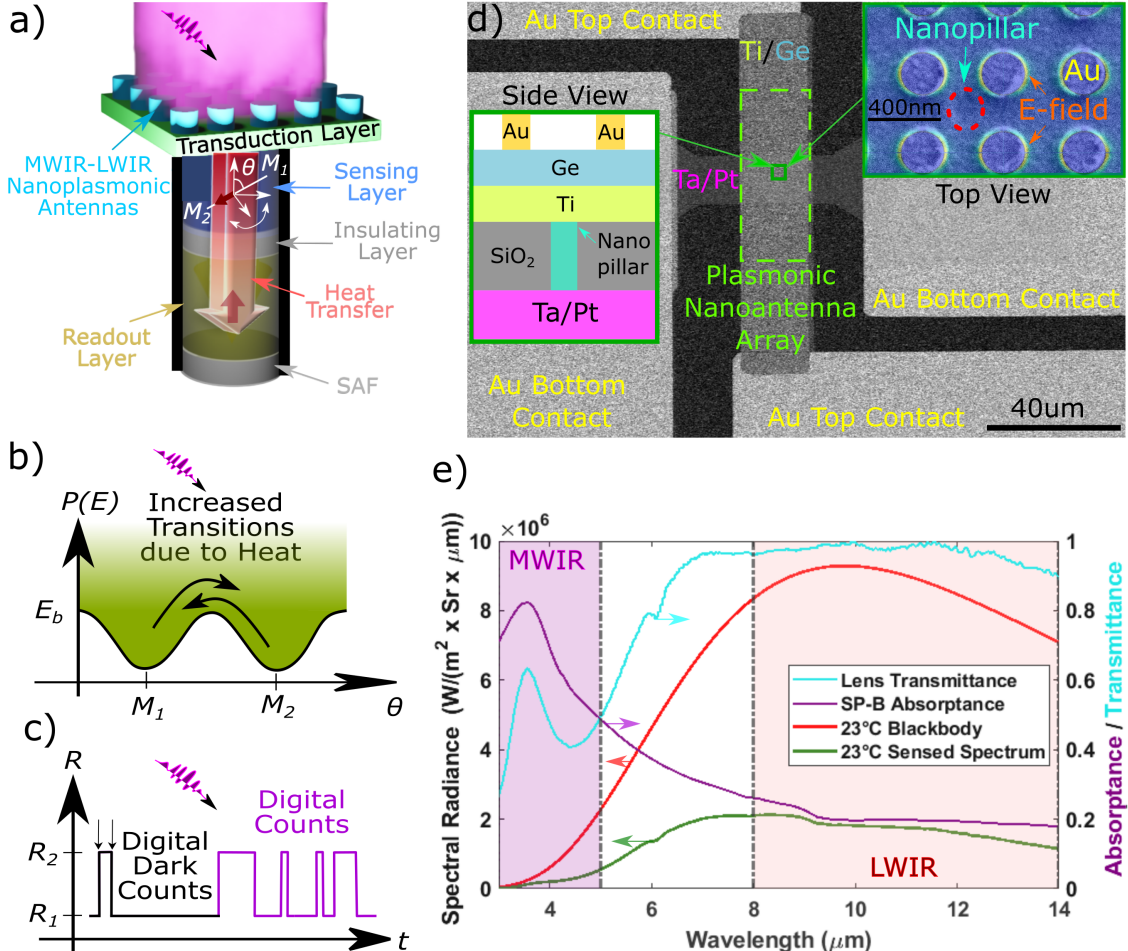


Figure 2: Schematic of SP-bolometer operation and spectral response. (a) Incident light is absorbed in the transduction layer, creating a thermal hotspot that diffuses through the bolometer. A synthetic antiferromagnet (SAF) adjacent to the sensing layer stabilizes the magnetic orientation. (b) Heat absorption increases the transition probability in the sensing layer, producing higher count rates. (c) The readout is obtained via resistance changes in the sensing layer. (d) SEM image of the SP-bolometer device with a plasmonic nanoantenna array atop a transduction layer (Ge/Ti). The inset on the right shows a top view of the nanoantenna array atop the SP-bolometer nanopillar, overlaid with a COMSOL-simulated electric field distribution. The left inset shows a side view of the SP-bolometer. (e) Spectral absorptance (purple), lens transmittance (cyan), blackbody radiation (red), and sensed spectrum (green) at a scene temperature of 23 °C. The nanoantenna array provides strong MWIR absorption and significant LWIR absorption, supporting broadband sensing despite the blackbody distribution.

survey of representative infrared detectors spanning the short-wave, mid-wave to long-wave spectral regions (SWIR–MWIR–LWIR), including both room-temperature and cooled technologies. Figure 1c compares the noise-equivalent temperature difference (NETD) versus wavelength for the surveyed detectors. NETD is the key metric for thermal sensitivity in thermal detectors. The SP bolometer is characterized with a broadband blackbody source, thus we use NETD rather than noise-equivalent power (NEP), which is typically defined for laser illumination. The SP bolometer reported here operates at room temperature across 3–14 μm with a noise-equivalent temperature difference (NETD) of 80–100 mK, establishing ultra-broadband thermal sensing performance. It outperforms state-of-the-art room-temperature detectors, including CNT (Carbon Nanotube),²⁹ BP/MoS₂ junction FET photodetectors (1.55–3.6 μm),³⁰ a-Si (Amorphous Silicon) LWIR detector,^{31,32} and VOx (Vanadium Oxide) LWIR detector.³⁴ Its performance is also comparable to leading cooled detectors, such as CQD (Colloidal Quantum Dot) detectors for NIR–MWIR with tunable band selection,³³ SLS (Strained Layer Superlattice),^{35,36} MCT (Mercury Cadmium Telluride),³⁷ and InSb (Indium Antimonide)³⁸ across their respective spectral bands (see Supplementary Section II).

Device Concept and Spintronic Transduction

We propose an ultra-broadband bolometer that integrates high-speed (30–120Hz), high thermal sensitivity (80–100mK) sensing with low power consumption (< 1mW) and a compact active area (0.09 μm^2). This solution addresses the full infrared range from MWIR to LWIR, utilizing the Sspintronic Poisson bolometer and a high-speed filter wheel for efficient spectral demonstration.

Stochastic Switching and Poisson Detection Regime

The SP-bolometer is a novel infrared sensor that utilizes a spintronic mechanism to achieve high sensitivity and rapid response. As shown in Figure 2a-c, the device operates through

thermally activated transitions between two stable magnetization states (M1 and M2) in the spintronic sensing layer.^{54–56} Discrete stochastic transitions occur due to an engineered small energy barrier (E_b) between these two states. Upon absorbing incident infrared light in the transduction layer (Figure 2a), a thermal hotspot is formed, which propagates heat through the bolometer. Heat increases the probability of transition in the sensing layer⁵⁷ (Figure 2b). This results in a higher transition rate, which is detected as resistance changes (Figure 2c). These changes are rapidly read out as digital signals, providing ultrafast response times. The addition of an adjacent synthetic antiferromagnet (SAF) stabilizes the readout orientation, ensuring reliable and consistent performance. Figure 2d shows the SEM image of the SP-bolometer device with a transduction layer modified with a plasmonic nanoantenna array. The inset of Figure 2d presents an SEM image of the nanoantenna array on the SP bolometer nanopillar, overlaid with the electric field distribution, highlighting field enhancement around the plasmonic nanoantennas.

Plasmonic Enhancement for Broadband Absorption

Integrating the nanoplasmonic antenna array into the SP bolometer enhances infrared absorption through localized plasmon resonance.^{14,58,59} The antennas enhance the electromagnetic field around the circular perimeter of the nanoantenna (inset of Figure 2d), leading to enhanced absorption of incident infrared radiation and improved overall device thermal sensitivity (see Supplementary Sections II). COMSOL simulation shows the field enhancement due to the nanoplasmonic antenna (Supplementary Figure 1). Our spectral measurements align well with COMSOL simulations, further validating the antenna design's effectiveness across the MWIR-LWIR spectrum (Supplementary Figure 2). This field enhancement is critical for achieving consistent performance across the full IR spectrum.

Figure 2e illustrates ellipsometry measurements of the nanoplasmonic antennas' absorbance (purple) peaks in the MWIR, while the blackbody spectral radiance (red) at 23°C peaks in the LWIR. The lens transmissivity (cyan) was measured by Fourier transform in-

frared (FTIR) spectroscopy. The design of the nanoplasmonic antenna ensures that the sensor effectively absorbs infrared radiation across the MWIR and LWIR bands, where Figure 2e (green) shows the IR sensed spectrum. The antenna design incorporates a transduction layer with 70 nm titanium (Ti) and 95 nm germanium (Ge), along with a refined array of 40 nm thick gold (Au) plasmonic nanoantennas, each with a 300 nm diameter and 320 nm center-to-center spacing. These antennas, arranged in a square lattice, optimize interaction with infrared radiation, providing robust ultra-broadband IR sensing (Supplementary Figure 3). In addition, the absorptance peak of the nanoplasmonic antenna can be tuned by adjusting the antenna design, such as its material composition and dimensions (Supplementary Figure 4). This flexibility allows the ultra-broadband SP bolometer to target specific IR applications with characteristic absorption spectra, such as gas sensing,⁶⁰ temperature estimation,⁶¹ and medical diagnostics.^{62,63}

Performance Benchmarking and Thermal Sensitivity

The thermal sensitivity of the IR detectors is characterized using the noise equivalent temperature difference (NETD),²⁸ a key metric representing the smallest detectable temperature difference. NETD is defined as:

$$NETD = \frac{V_n}{dV/dT} \quad (3)$$

where V_n is the standard deviation of the detector signal at T_0 (23°C in our measurements) and dV/dT is the signal change per degree of temperature variation.

Broadband NETD measurements of the SP-bolometer were conducted using an ultra-stable blackbody source ($\approx 1\text{mK}$ stability) and a broadband ZnSe IR lens with an f/0.5 aperture, yielding 81.2mK under 0Oe magnetic field and 575 μA bias (Figure 3a–b). Using the NETD metric, the SP-bolometer was compared to a representative LWIR VO_x microbolometer (analog, 300K, FLIR A325sc) and MWIR InSb photodiode (analog, 77K, Telops Spark

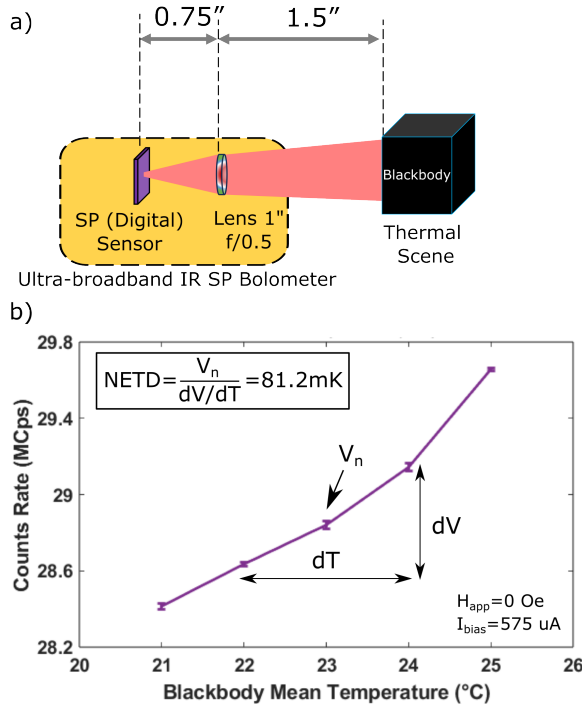


Figure 3: Broadband NETD measurement setup and response of the SP-bolometer. (a) Schematic of the broadband NETD measurement setup for the SP-bolometer, including ultra-stable blackbody source and broadband ZnSe lens (f/0.5). (b) Broadband NETD response of the SP-bolometer without optical filtering, measured at varying blackbody temperatures, demonstrating a NETD of approximately 81mK under 0Oe magnetic field and 575 μ A bias.

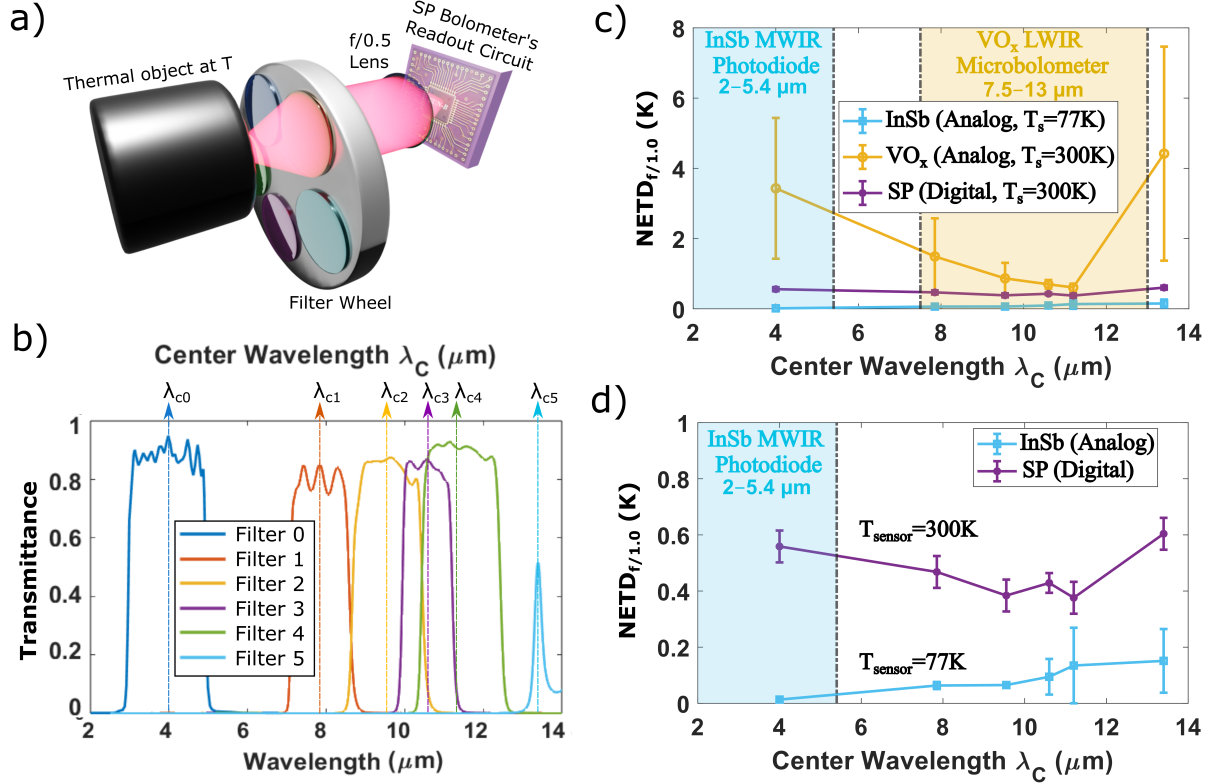


Figure 4: Consistent MWIR–LWIR NETD performance of the SP-bolometer compared with state-of-the-art infrared cameras. (a) Experimental setup for ultra-broadband MWIR–LWIR NETD measurements using the Spintronic Poisson (SP) bolometer with a high-speed filter wheel. (b) Spectral transmittance of the optical filters used in the NETD measurements. (c) Spectral comparison of NETD for a representative state-of-the-art uncooled analog VO_x microbolometer (analog, LWIR, 300K, FLIR A325sc) in blue color, InSb photodiode (analog, MWIR, 77K, Telops Spark M150) in orange color, and broadband SP-bolometer (purple). The InSb photodiode performs better with lower NETD across the $3\mu\text{m}$ to $13.5\mu\text{m}$ range. However, the SP-bolometer's NETD is comparable to the InSb photodiode and notably outperforms the VO_x microbolometer across all bands. (d) Zoomed-in view of (c), highlighting differences in NETD between the SP bolometer and InSb photodiode. Error bars for the VO_x microbolometer increase at wavelengths farther from $10.6\mu\text{m}$, likely due to the LWIR lens's optical bandwidth limitations. T_s : Sensor Temperature. The NETD values are normalized to an f -number of $f/1.0$, where $\text{NETD}_{f/1} = \text{NETD}/(f/\#)^2$. The f -numbers are $f/\# = 0.5$ for the SP-bolometer, $f/\# = 0.6$ for the VO_x microbolometer, and $f/\# = 2.3$ for the InSb photodiode.

M150). For band-specific characterization, a high-speed MWIR–LWIR filter wheel enabled rapid selection of MWIR and LWIR bands at 30Hz, while the blackbody provided controlled thermal illumination from 21°C to 25°C in 1°C increments. The SP-bolometer signal was stabilized using an adaptive algorithm,⁶⁴ which dynamically removes outliers via a 33ms moving mean, ensuring accurate NETD measurements without compromising the 30Hz frame rate.

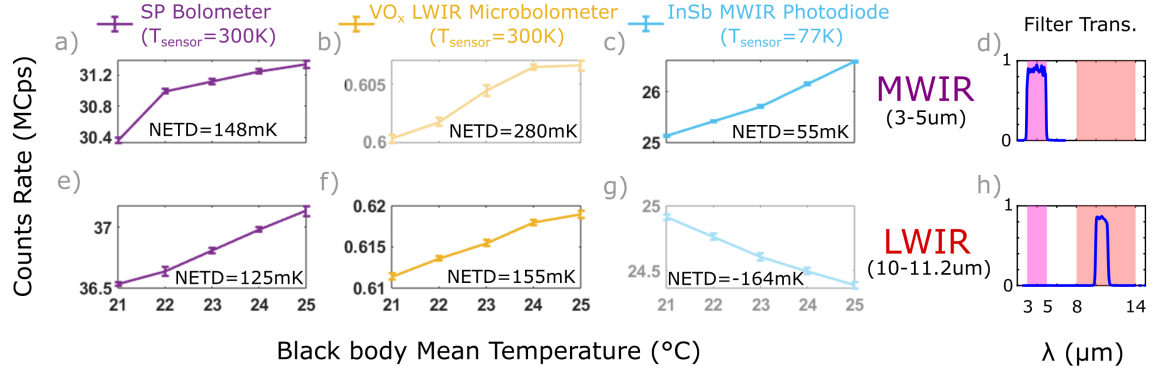


Figure 5: Consistent MWIR-LWIR sensor response of the SP-bolometer compared with state-of-the-art cameras. (a) SP-bolometer response (count rate) to the MWIR band (3 – 5 μm). (b) VO_x microbolometer (analog, LWIR, 300K, FLIR A325sc) response (count rate) to the MWIR band (3 – 5 μm). (c) InSb photodiode (analog, MWIR, 77K, Telops Spark M150) response (count rate) to the MWIR band (3 – 5 μm). (d) MWIR filter transmittance (3 – 5 μm). (e) SP-bolometer response (count rate) to the LWIR band (10 – 11.2 μm). (f) VO_x microbolometer (analog, LWIR, 300K, FLIR A325sc) response (count rate) to the LWIR band (10 – 11.2 μm). (g) InSb photodiode (analog, MWIR, 77K, Telops Spark M150) response (count rate) to the LWIR band (10 – 11.2 μm). (h) LWIR filter transmittance (10 – 11.2 μm). T_s : sensor temperature. The SP-bolometer exhibits a consistent response across MWIR and LWIR bands, performing comparably to the cooled InSb photodiode in MWIR and outperforming the VO_x microbolometer across LWIR. Error bars represent the standard deviation from five measurements with 33 ms integration time.

The experimental setup (Figure 4a) ensured fair comparison across sensors. We used a broadband ZnSe lens (f/0.5) for the SP-bolometer, its built-in f/0.6 lens for the VO_x microbolometer, while the InSb photodiode was equipped with a built-in f/2.3 lens. To account for differences in optics, NETD was normalized according to lens f-number (f/#):

$$NETD_{f/1.0} = \frac{NETD}{(f/\#)^2} \quad (4)$$

Figure 4c presents normalized NETD results for the SP-bolometer across MWIR and

LWIR bands, showing performance comparable to the InSb photodiode (analog, MWIR, 77K, Telops Spark M150) and superior to the VO_x microbolometer (analog, LWIR, 300K, FLIR A325sc) across all bands. Error bars indicate standard deviation over five measurements, reflecting optical bandwidth limitations for both VO_x microbolometer (centered at $10.6\mu\text{m}$, yellow shaded area) and InSb photodiode (centered at $4\mu\text{m}$, blue shaded area).

Figure 5 presents a comparative analysis of sensor responses (count rate), illustrating the SP-bolometer's MWIR response with an MWIR filter (filter 0, Figure 5a) and LWIR response with LWIR filters (filter 3, Figure 5e). Filter transmissivity is shown in Figures 5d (MWIR) and 5h (LWIR). The SP-bolometer demonstrates performance comparable to the cooled InSb photodiode in MWIR while exceeding that of the VO_x microbolometer across all bands. The InSb photodiode exhibits the strongest MWIR response but displays a monotonically decreasing count rate with increasing scene temperature in LWIR, reflecting that the detector and optics are not designed for this band.

The SP-bolometer is compatible with large-scale fabrication and system integration. Its planar, lithography-based architecture can be implemented using standard CMOS-compatible processes,^{65–67} enabling wafer-level scalability and array-level deployment. The low-bias, room-temperature operation further supports seamless integration with on-chip readout and neuromorphic processing circuits for real-time, energy-efficient thermal imaging.⁶⁸ Future work will focus on extending the operational bandwidth beyond the $0.8\text{--}14\mu\text{m}$ range (toward the THz regime) through absorber and antenna engineering. Another promising direction is integrating multispectral filtering to enable intelligent, adaptive sensing and to support heat-assisted detection and ranging (HADAR)²⁵ applications. These developments position the SP-bolometer as a foundational platform for next-generation ultra-broadband infrared imaging and perception technologies.

Conclusion

This work demonstrates the design and experimental characterization of the ultra-broadband SP-bolometer, a non-cryogenic infrared detector with high thermal sensitivity across the MWIR–LWIR spectrum. The SP-bolometer achieves a broadband NETD of 81 mK under ambient operation (300 K) with minimal biasing requirements (0 Oe, 575 μ A), demonstrating high thermal sensitivity. Comparative characterization shows that the SP-bolometer response is comparable to that of a InSb photodiode (analog, MWIR, 77K) and surpasses that of the VO_x microbolometer (analog, LWIR, 300K) across all spectral bands. By encoding temperature in discrete Poisson-distributed events rather than continuous analog signals, the SP-bolometer operates natively under thermal fluctuations, effectively turning noise into a measurable signal and establishing a fundamentally new detection paradigm. The integrated nanoplasmonic antennas enable efficient and broadband infrared absorption, while the adaptive algorithm minimizes signal fluctuations to maintain high measurement accuracy at 30 Hz. This demonstration establishes the SP-bolometer as a compact, energy-efficient, and ultra-broadband infrared sensor that advances uncooled detection technologies for applications in autonomous systems, environmental sensing, and biomedical diagnostics. Its room-temperature operation, CMOS-compatible planar design, and low-power architecture further enable scalable array integration and intelligent on-chip infrared imaging.

Acknowledgement

We would like to thank Dr. Tiffany Santos from Western Digital for providing the thin films used to fabricate the SP bolometer devices in this work. This work was partially supported by an Elmore Chaired Professorship at Purdue University.

Supporting Information Available

See Supplemental document for supporting content, available online.

References

- (1) Rogalski, A. Progress in focal plane array technologies. *Progress in Quantum Electronics* **2012**, *36*, 342–473.
- (2) Razeghi, M.; Nguyen, B.-M. Advances in mid-infrared detection and imaging: a key issues review. *Reports on Progress in Physics* **2014**, *77*, 082401.
- (3) Rogalski, A. Infrared detectors: status and trends. *Progress in quantum electronics* **2003**, *27*, 59–210.
- (4) Rogalski, A. HgCdTe infrared detectors: historical prospect. Quantum Sensing: Evolution and Revolution from Past to Future. 2003; pp 431–442.
- (5) Zha, J.; Luo, M.; Ye, M.; Ahmed, T.; Yu, X.; Lien, D.-H.; He, Q.; Lei, D.; Ho, J. C.; Bullock, J.; others Infrared photodetectors based on 2D materials and nanophotonics. *Advanced Functional Materials* **2022**, *32*, 2111970.
- (6) Hafiz, S. B.; Scimeca, M. R.; Zhao, P.; Paredes, I. J.; Sahu, A.; Ko, D.-K. Silver selenide colloidal quantum dots for mid-wavelength infrared photodetection. *ACS Applied Nano Materials* **2019**, *2*, 1631–1636.
- (7) Rogalski, A.; Kopytko, M.; Hu, W.; Martyniuk, P. Infrared HOT photodetectors: status and outlook. *Sensors* **2023**, *23*, 7564.
- (8) Wang, B.; Lai, J.; Li, H.; Hu, H.; Chen, S. Nanostructured vanadium oxide thin film with high TCR at room temperature for microbolometer. *Infrared Physics & Technology* **2013**, *57*, 8–13.

(9) Yadav, P. K.; Yadav, I.; Ajitha, B.; Rajasekar, A.; Gupta, S.; Reddy, Y. A. K. Advancements of uncooled infrared microbolometer materials: A review. *Sensors and Actuators A: Physical* **2022**, *342*, 113611.

(10) Das, A.; Mah, M. L.; Hunt, J.; Talghader, J. J. Thermodynamically limited uncooled infrared detector using an ultra-low mass perforated subwavelength absorber. *Optica* **2023**, *10*, 1018–1028.

(11) Kazanskiy, N.; Khabibullin, R.; Nikonorov, A.; Khonina, S. A Comprehensive Review of Remote Sensing and Artificial Intelligence Integration: Advances, Applications, and Challenges. *Sensors* **2025**, *25*, 5965.

(12) Dong, Y.; Huang, W.; Li, H.; Han, L. Advancements in agricultural monitoring with AI enhanced remote sensing techniques. 2025.

(13) Hagenaars, E.; Pandharipande, A.; Murthy, A.; Leus, G. Single-pixel thermopile infrared sensing for people counting. *IEEE Sensors Journal* **2020**, *21*, 4866–4873.

(14) Tan, X.; Zhang, H.; Li, J.; Wan, H.; Guo, Q.; Zhu, H.; Liu, H.; Yi, F. Non-dispersive infrared multi-gas sensing via nanoantenna integrated narrowband detectors. *Nature communications* **2020**, *11*, 5245.

(15) Jang, W.-Y.; Ku, Z.; Jeon, J.; Kim, J. O.; Lee, S. J.; Park, J.; Noyola, M. J.; Urbas, A. Experimental demonstration of adaptive infrared multispectral imaging using plasmonic filter array. *Scientific reports* **2016**, *6*, 34876.

(16) Zhu, H.; Li, Q.; Tao, C.; Hong, Y.; Xu, Z.; Shen, W.; Kaur, S.; Ghosh, P.; Qiu, M. Multispectral camouflage for infrared, visible, lasers and microwave with radiative cooling. *Nature communications* **2021**, *12*, 1805.

(17) Qin, B.; Zhu, Y.; Zhou, Y.; Qiu, M.; Li, Q. Whole-infrared-band camouflage with dual-band radiative heat dissipation. *Light: Science & Applications* **2023**, *12*, 246.

(18) Wilson, R. H.; Nadeau, K. P.; Jaworski, F. B.; Tromberg, B. J.; Durkin, A. J. Review of short-wave infrared spectroscopy and imaging methods for biological tissue characterization. *Journal of biomedical optics* **2015**, *20*, 030901–030901.

(19) Rogalski, A.; Martyniuk, P.; Kopytko, M.; Hu, W. Trends in performance limits of the HOT infrared photodetectors. *Applied Sciences* **2021**, *11*, 501.

(20) Huang, L.; Han, Z.; Wirth-Singh, A.; Saragadam, V.; Mukherjee, S.; Fröch, J. E.; Tanguy, Q. A.; Rollag, J.; Gibson, R.; Hendrickson, J. R.; others Broadband thermal imaging using meta-optics. *Nature Communications* **2024**, *15*, 1662.

(21) Wang, X.; Yang, Z.; Bao, F.; Sentz, T.; Jacob, Z. Spinning metasurface stack for spectro-polarimetric thermal imaging. *Optica* **2024**, *11*, 73–80.

(22) Boiko, D. A.; Korabelnikova, V. A.; Gordeev, E. G.; Ananikov, V. P. Integration of thermal imaging and neural networks for mechanical strength analysis and fracture prediction in 3D-printed plastic parts. *Scientific Reports* **2022**, *12*, 8944.

(23) Hatzell, K. B.; Chen, X. C.; Cobb, C. L.; Dasgupta, N. P.; Dixit, M. B.; Marbella, L. E.; McDowell, M. T.; Mukherjee, P. P.; Verma, A.; Viswanathan, V.; others Challenges in lithium metal anodes for solid-state batteries. *ACS Energy Letters* **2020**, *5*, 922–934.

(24) Yang, Y.; Jiang, J.; Zeng, J.; Chen, Z.; Zhu, X.; Shi, Y. CH₄, C₂H₆, and CO₂ multi-gas sensing based on portable mid-infrared spectroscopy and PCA-BP algorithm. *Sensors* **2023**, *23*, 1413.

(25) Bao, F.; Wang, X.; Sureshbabu, S. H.; Sreekumar, G.; Yang, L.; Aggarwal, V.; Boddeti, V. N.; Jacob, Z. Heat-assisted detection and ranging. *Nature* **2023**, *619*, 743–748.

(26) Vincent, J. D.; Hodges, S.; Vampola, J.; Stegall, M.; Pierce, G. *Fundamentals of infrared and visible detector operation and testing*; John Wiley & Sons, 2015.

(27) Macleod, H. A.; Macleod, H. A. *Thin-film optical filters*; CRC press, 2010.

(28) Rogalski, A. *Infrared and terahertz detectors*; CRC press, 2019.

(29) Liu, Y.; Yin, J.; Wang, P.; Hu, Q.; Wang, Y.; Xie, Y.; Zhao, Z.; Dong, Z.; Zhu, J.-L.; Chu, W.; others High-performance, ultra-broadband, ultraviolet to terahertz photodetectors based on suspended carbon nanotube films. *ACS applied materials & interfaces* **2018**, *10*, 36304–36311.

(30) Shu, X.; Wu, J.; Zhong, F.; Zhang, X.; Fu, Q.; Han, X.; Zhang, J.; Lu, J.; Ni, Z. High-responsivity, high-detectivity, broadband infrared photodetector based on MoS₂/BP/MoS₂ junction field-effect transistor. *Applied Physics Letters* **2024**, *124*.

(31) Rogalski, A.; Martyniuk, P.; Kopytko, M. Challenges of small-pixel infrared detectors: a review. *Reports on Progress in Physics* **2016**, *79*, 046501.

(32) Lynred Athena 1920 - Uncooled 12 μm infrared detector (1920 x 1080). Lynred, 2023; Grenoble, France.

(33) Tang, X.; Ackerman, M. M.; Chen, M.; Guyot-Sionnest, P. Dual-band infrared imaging using stacked colloidal quantum dot photodiodes. *Nature photonics* **2019**, *13*, 277–282.

(34) Lynred PICO1024Gen2 - Uncooled 10 μm infrared detector (1024 x 768). Lynred, 2024; Grenoble, France.

(35) Lee, H.-J.; Eom, J. H.; Jung, H. C.; Kang, K.-K.; Ryu, S. M.; Jang, A.; Kim, J. G.; Kim, Y. H.; Jung, H.; Kim, S. H.; others Design and performance of dual-band MWIR/LWIR focal plane arrays based on a type-II superlattice nBn structure. *Opto-Electronics Review* **2023**, *31*.

(36) IRCameras, LLC IRC906SLS Broadband Infrared Camera Data Sheet. IRCameras, LLC, 2018; Santa Barbara, CA.

(37) DRS, L. Condor HD Dual Waveband Infrared Detector Data Sheet. Leonardo DRS, 2024; Arlington, VA.

(38) FLIR Systems, I. FLIR A6750sc Mid-Wave Infrared Camera Data Sheet. FLIR Systems, Inc., 2014; Wilsonville, OR.

(39) Figgemeier, H.; Ames, C.; Beetz, J.; Breiter, R.; Eich, D.; Hanna, S.; Mahlein, K.-M.; Schallenberg, T.; Sieck, A.; Wenisch, J. High-performance SWIR/MWIR and MWIR/MWIR bispectral MCT detectors by AIM. *Infrared Technology and Applications XLIV*. 2018; pp 120–131.

(40) Cervera, C.; Baier, N.; Gravrand, O.; Mollard, L.; Lobre, C.; Destefanis, G.; Zanatta, J.; Boulade, O.; Moreau, V. Low-dark current p-on-n MCT detector in long and very long-wavelength infrared. *Infrared Technology and Applications XLI*. 2015; pp 615–624.

(41) Haddadi, A.; Dehzangi, A.; Chevallier, R.; Adhikary, S.; Razeghi, M. Bias-selectable nBn dual-band long-/very long-wavelength infrared photodetectors based on InAs/InAs_{1-x}Sb_x/AlAs_{1-x}Sb_x type-II superlattices. *Scientific reports* **2017**, *7*, 3379.

(42) Richards, P. L. Bolometers for infrared and millimeter waves. *Journal of Applied Physics* **1994**, *76*, 1–24.

(43) Martini, P.; Kanellopoulos, K.; Emminger, S.; Luhmann, N.; Piller, M.; West, R. G.; Schmid, S. Uncooled thermal infrared detection near the fundamental limit using a silicon nitride nanomechanical resonator with a broadband absorber. *Communications Physics* **2025**, *8*, 166.

(44) Bielecki, Z.; Mikolajczyk, J.; Wojtas, J. A Review of Thermal Detectors of THz Radiation Operated at Room Temperature. *Sensors* **2024**, *24*, 6784.

(45) Shynk, J. J. *Probability, random variables, and random processes: theory and signal processing applications*; John Wiley & Sons, 2012.

(46) Van Trees, H. L. *Detection, estimation, and modulation theory, part I: detection, estimation, and linear modulation theory*; John Wiley & Sons, 2004.

(47) Kingman, J. F. C. *Poisson processes*; Clarendon Press, 1992; Vol. 3.

(48) Van Kampen, N. G. *Stochastic processes in physics and chemistry*; Elsevier, 1992; Vol. 1.

(49) Pinsky, M.; Karlin, S. *An introduction to stochastic modeling*; Academic press, 2010.

(50) Lehmann, E. L.; Casella, G. *Theory of point estimation*; Springer, 1998.

(51) Bauer, L.; Deka, A.; Mousa, M. A.; Gupta, S.; He, D.; Huang, S.; Prasad, B.; Santos, T.; Ray, B.; Jacob, Z. Exploiting Spintronics at Room Temperature for Long-Wave Infrared Nanophotonic Digital Bolometers. *Nano Letters* **2025**, *25*, 5599–5608.

(52) Yu, L.; Guo, Y.; Zhu, H.; Luo, M.; Han, P.; Ji, X. Low-cost microbolometer type infrared detectors. *Micromachines* **2020**, *11*, 800.

(53) Jung, J.; Kim, M.; Kim, C.-H.; Kim, T. H.; Park, S. H.; Kim, K.; Cho, H. J.; Kim, Y.; Kim, H. Y.; Oh, J. S. Improved responsivity of an a-Si-based micro-bolometer focal plane array with a SiNx membrane layer. *J. Sens. Sci. Technol* **2022**, *31*, 366–370.

(54) Hayakawa, K.; Kanai, S.; Funatsu, T.; Igarashi, J.; Jinnai, B.; Borders, W.; Ohno, H.; Fukami, S. Nanosecond random telegraph noise in in-plane magnetic tunnel junctions. *Physical review letters* **2021**, *126*, 117202.

(55) Laughlin, D. E. Magnetic transformations and phase diagrams. *Metallurgical and Materials Transactions A* **2019**, *50*, 2555–2569.

(56) Coffey, W. T.; Kalmykov, Y. P. Thermal fluctuations of magnetic nanoparticles: Fifty years after Brown. *Journal of Applied Physics* **2012**, *112*.

(57) Kanai, S.; Hayakawa, K.; Ohno, H.; Fukami, S. Theory of relaxation time of stochastic nanomagnets. *Physical Review B* **2021**, *103*, 094423.

(58) Su, J.; Li, C.; Xiao, J.; Kong, J.; Hu, P.; Lu, C.; Zhu, L. Boosting infrared absorption through surface plasmon resonance enhanced HgCdTe microcavity. *Journal of Applied Physics* **2023**, *134*.

(59) Debu, D. T.; Bauman, S. J.; French, D.; Churchill, H. O.; Herzog, J. B. Tuning infrared plasmon resonance of black phosphorene nanoribbon with a dielectric interface. *Scientific reports* **2018**, *8*, 3224.

(60) Krzempek, K. A review of photothermal detection techniques for gas sensing applications. *Applied Sciences* **2019**, *9*, 2826.

(61) Gabriel, R.; Keller, S.; Matthes, J.; Waibel, P.; Keller, H.; Hinz, S. Infrared measurements and estimation of temperature in the restrictive scope of an industrial cement plant. *ISPRS Annals of the Photogrammetry, Remote Sensing and Spatial Information Sciences* **2018**, *4*, 53–60.

(62) Lahiri, B. B.; Bagavathiappan, S.; Jayakumar, T.; Philip, J. Medical applications of infrared thermography: a review. *Infrared physics & technology* **2012**, *55*, 221–235.

(63) Mousa, M. A.; Rafat, N. H.; Saleh, A. A. Toward spectrometerless instant Raman identification with tailored metasurfaces-powered guided-mode resonances (GMR) filters. *Nanophotonics* **2021**, *10*, 4567–4577.

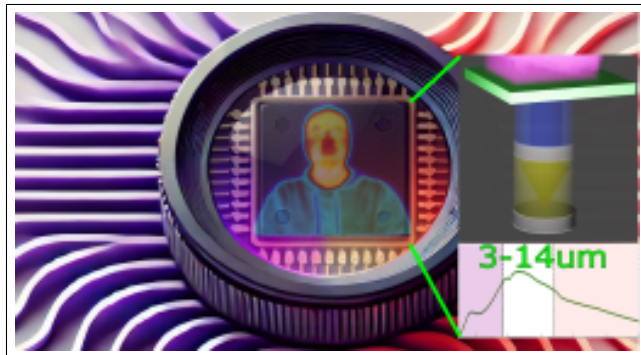
(64) Ma, Y.; Gemmell, N.; Pearce, E.; Oulton, R.; Phillips, C. Eliminating thermal infrared background noise by imaging with undetected photons. *Physical Review A* **2023**, *108*, 032613.

(65) Suhail, H.; He, H.; Yang, J.; Shu, Q.; Wang, C.-Y.; Yang, S.-Y.; Hsin, Y.-C.; Shih, C.-Y.; Lee, H.-H.; Wu, D.; others The first CMOS-integrated voltage-controlled MRAM

with 0.7 ns switching time. 2023 International Electron Devices Meeting (IEDM). 2023; pp 1–4.

- (66) Barla, P.; Shivarama, H.; Deepa, G.; Ujjwal, U. Design and Assessment of Hybrid MTJ/CMOS Circuits for In-Memory-Computation. *Journal of Low Power Electronics and Applications* **2024**, *14*, 3.
- (67) Singh, U.; Bauer, L.; Deka, A.; Mousa, M.; He, D.; Gupta, S.; Prasad, B.; Jacob, Z. Long wave infrared detection using probabilistic spintronic bolometer arrays. *arXiv preprint arXiv:2510.06519* **2025**,
- (68) Mousa, M. A.; Singh, U.; Bauer, L.; Deka, A.; Jacob, Z. Neural bolometers: Designing next-generation infrared thermal imagers with in-pixel neuromorphic computing. *Phys. Rev. Appl.* **2025**, *24*, 064044.

TOC Graphic



An uncooled spintronic Poisson bolometer integrates nanoplasmonic antennas for ultra-broadband MWIR–LWIR sensing, achieving high thermal sensitivity via stochastic transduction.